NRC·CNRC

NRC Publications Archive
Archives des publications du CNRC

Calibration of an internal-length standard by angle-stepping gap interferometry

Leroux, Ian D.; Hunter, Tyler J.; Reain, Gregory C.; Eves, Brian J.

This publication could be one of several versions: author's original, accepted manuscript or the publisher's version. / La version de cette publication peut être l'une des suivantes : la version prépublication de l'auteur, la version acceptée du manuscrit ou la version de l'éditeur.

For the publisher's version, please access the DOI link below./ Pour consulter la version de l'éditeur, utilisez le lien DOI ci-dessous.

Publisher's version / Version de l'éditeur:

https://doi.org/10.1088/1681-7575/adb753

Metrologia, 62, 2, pp. 1-9, 2025-03-04

NRC Publications Archive Record / Notice des Archives des publications du CNRC :

https://nrc-publications.canada.ca/eng/view/object/?id=7f23ac7e-c3cd-44f4-b5e6-01d0fd3facd7

https://publications-cnrc.canada.ca/fra/voir/objet/?id=7f23ac7e-c3cd-44f4-b5e6-01d0fd3facd7

Access and use of this website and the material on it are subject to the Terms and Conditions set forth at

https://nrc-publications.canada.ca/eng/copyright

READ THESE TERMS AND CONDITIONS CAREFULLY BEFORE USING THIS WEBSITE.

L'accès à ce site Web et l'utilisation de son contenu sont assujettis aux conditions présentées dans le site

https://publications-cnrc.canada.ca/fra/droits

LISEZ CES CONDITIONS ATTENTIVEMENT AVANT D'UTILISER CE SITE WEB.

Questions? Contact the NRC Publications Archive team at PublicationsArchive-ArchivesPublications@nrc-cnrc.gc.ca. If you wish to email the authors directly, please see the first page of the publication for their contact information.

Vous avez des questions? Nous pouvons vous aider. Pour communiquer directement avec un auteur, consultez la première page de la revue dans laquelle son article a été publié afin de trouver ses coordonnées. Si vous n'arrivez pas à les repérer, communiquez avec nous à PublicationsArchive-ArchivesPublications@nrc-cnrc.gc.ca.

National Research Council Canada | Conseil national de recherches Canada

Canada

OPEN ACCESS
IOP Publishing | Bureau International des Poids et Mesures Metrologia
Metrologia **62** (2025) 025007 (9pp) https://doi.org/10.1088/1681-7575/adb753

Calibration of an internal-length standard by angle-stepping gap interferometry

Ian D Leroux*, **Tyler J Hunter, Gregory C Reain and Brian J Eves**

Metrology Research Centre, National Research Council Canada, K1A 0R6 Ottawa, Ontario, Canada

E-mail: Ian.Leroux@nrc-cnrc.gc.ca

Received 22 October 2024, revised 27 January 2025
Accepted for publication 18 February 2025
Published 4 March 2025

Abstract

We demonstrate a simple interferometric method for calibrating the length of an uncoated Fabry-Pérot etalon, using a rotary analog of phase-stepping interferometry. The interferometric method is designed to realize nearly the same measurand as a subsequent measurement in a tactile instrument. The estimated expanded uncertainty of 4 nm for the optical calibration, together with the well-matched measurands, make the etalon a promising transfer standard for the calibration of bidirectional corrections in tactile probing systems.

Keywords: Fabry-Pérot etalon, phase-stepping interferometry, bidirectional correction, probe diameter, point-to-point length

1. Motivation

Bidirectional length measurements, made between material surfaces that face toward or away from each other, require a correction for the effective size of the probing system. This bidirectional correction fixes the zero position of the length scale, where differently-oriented surfaces would be deemed to coincide. For example, bidirectional corrections are required when measuring diameters of spherical or cylindrical objects, gap widths, or thicknesses of manufactured parts.

The bidirectional correction can be determined using a calibrated end standard such as a gauge block, by comparing the calibrated length to the indicated length between gauging points on opposite faces. Ideally, the difference between these two lengths is the effective probe diameter of the measuring instrument. When using a conventionally-calibrated gauge block, however, the accuracy of this comparison is limited by a measurand mismatch [1]. The calibrated length of the gauge block, as specified in ISO 3650 [2], is a unidirectional length between a point on one gauging surface and an auxiliary plane wrung to the opposite surface (figure 1(a)). The measurand typically realized in a tactile instrument, however, is a point-to-point length with a different sensitivity to the form of one of the gauging faces—because no auxiliary plane is used—and without any wringing interface (figure 1(b)). If an internal-length transfer standard is wanted, e.g. for a direct mechanical comparison with a ring gauge, it is often created by wringing cap blocks to the ends of a gauge block (figure 1(c)). In this case there is an additional measurand mismatch due to the Abbe offset between the calibrated central length of the gauge block and the tactile instrument's measurement line outside the gauge block. These measurand mismatches contribute significantly to the uncertainty of the bidirectional correction [3, 4]. For external length measurements, several specialized transfer standards have been developed to mitigate these problems, including gauge blocks calibrated by double-ended

* Author to whom any correspondence should be addressed.

Original Content from this work may be used under the terms of the Creative Commons Attribution 4.0 licence. Any further distribution of this work must maintain attribution to the author(s) and the title of the work, journal citation and DOI.

© His Majesty the King in Right of Canada, as represented by the Minister of Innovation, Science and Industry, 2025

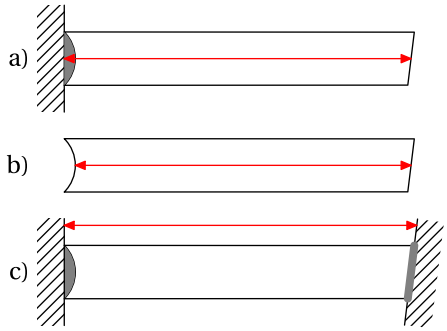

Figure 1. Measurand mismatches when using gauge blocks to establish bidirectional corrections: (a) defined central length of the gauge block as calibrated. (b) and (c) External and internal point-to-point lengths measured by a tactile probe. Shaded regions indicate wrung interfaces. Hatched regions indicate auxiliary planes (platens or cap blocks).

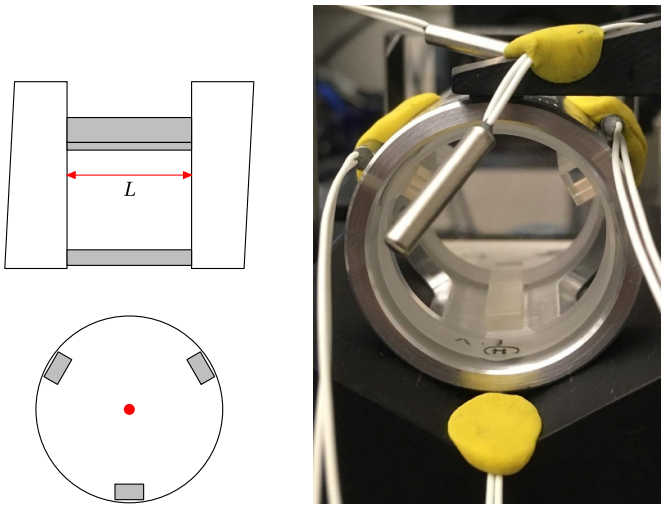

Figure 2. Internal-length transfer standard. Left: schematic side and end views of the etalon, with the fused-silica plates in white and the ultra-low-expansion pillars in gray. The wedge angle of the end plates has been exaggerated for clarity. The red arrow marks the measurand L, the gap length between inner etalon surfaces on the centerline of the artifact. Right: photograph of the artifact, with three thermistors attached to the housing and another two suspended in the air nearby.

interferometry to realize a point-to-point measurand [1] and two-point diameters of precision spheres [1, 5].

Here we present an internal end standard, i.e. one where the gauging surfaces face toward each other rather than outward, designed to minimize measurand differences between interferometric calibration and subsequent use in a tactile probing instrument such as a coordinate measuring machine (CMM). The calibrated internal length is suited to direct comparison measurements of ring or bore diameter. We also present a calibration scheme which can be viewed as a rotary analog of phase-stepping interferometry (PSI) [6–9]. We note that an artifact similar to the one presented here, described as a 'transparent, fused-silica box with 10 mm spacing', has been used for ring diameter calibrations at NPL, but with a different calibration scheme based on white-light interferometry [10, 11].

2. Artifact

The end standard used in this work is an air-gapped Fabry-Pérot etalon (figure 2). Such etalons have been used in dimensional metrology at least since the 1906 redetermination of the wavelength of the red cadmium line with respect to the metre [12], but are usually treated as purely optical artifacts. Here we require that the etalon also serve as a mechanical gauge for a tactile probe.

The etalon is formed by two uncoated fused-silica plates, each with a 30′ wedge angle, whose inner surfaces are maintained parallel to each other and 20 mm apart by three pillars of ultra-low-expansion glass spaced around their circumference. The pillars are optically contacted to the end plates to produce a rigid assembly, which in turn is flexibly mounted in a protective aluminium housing. Three ports in the housing allow a CMM probe to reach most of the inner surfaces of the etalon. The gauging surfaces are separated by an air gap, i.e. a medium with a well-characterized index of refraction, allowing a direct interferometric calibration along the same line that a tactile instrument will measure. The parallelism of the gauging surfaces, which is checked interferometrically, reduces the impact of any residual errors in locating the interferometric measurement line and tactile gauging points. The same rigid assembly is used for the interferometric calibration and for mechanical measurements, without adding or removing any wringing interfaces, avoiding uncertainties due to assembly or disassembly of a composite artifact. Phase shifts that displace the effective plane of optical reflection from the mechanical surface detected by a tactile probe are avoided by the use of uncoated, highly-polished dielectric gauging surfaces. Compared to a gauge block used as a transfer standard, uncertainties associated with Abbe offsets, wringing, and phase corrections are thus much reduced in the etalon.

3. Optical setup

A Fabry-Pérot etalon is already an interferometer, reflecting or transmitting light depending on the optical path length between the two end plates. Consider a plane wave with wavelength λ incident on an etalon whose two plates are separated by a gap L. The extra distance traveled by a wave reflected from the second surface compared to one reflected from the first surface, expressed in wavelengths, is

$$\frac{2L}{\lambda}\cos\theta, \tag{1}$$

where θ is the angle between the propagation direction of the light and the axis normal to the etalon surfaces. Any of the three parameters L, λ and θ can be varied in order to see the

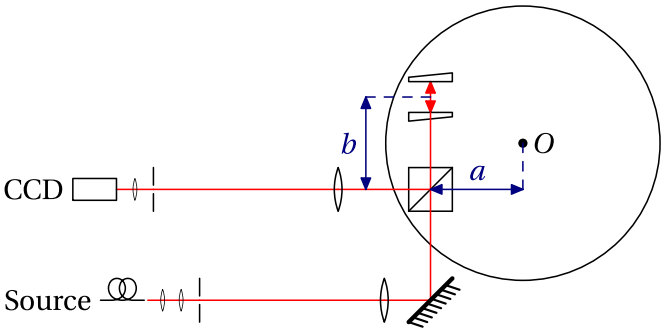

Figure 3. Setup for angle-stepping interferometry. Monochromatic light, delivered via single-mode fiber, is focused through a pinhole, collimated, and directed at the artifact through a beamsplitter. Light reflected by the artifact is deflected by the beamsplitter to a separate imaging telescope which collects it, filters out stray light with an iris, and images the artifact onto a CCD camera. O is the center of rotation of the table on which both artifact and beam-splitter are mounted. The beam offset a from the center of rotation and the spacing b between artifact center and beam-splitter centre should be approximately equal to minimize image translation as the table rotates.

interference fringe. L can be varied by deforming the artifact or by introducing a slight angle between the end faces so that their spacing varies with transverse position. Both approaches introduce additional uncertainty in the measurand definition. λ can be varied by changing the frequency of the light source or by varying the ambient air pressure and thus the index of refraction, at some cost in apparatus complexity. θ is traditionally varied using an uncollimated light source and an imaging system focused at infinity to view Haidinger fringes, i.e. the rings of constructive and destructive interference for light rays of equal inclination to the axis of the etalon [12, 13]. This is simple and effective, but it measures an average gap between the plates across the whole illuminating beam, since light rays of a given inclination appear together in the far-field fringe pattern no matter their transverse position at the etalon. We would prefer to measure the gap as a function of transverse position, producing a map of etalon plate separation, both to check the flatness and parallelism of the etalon surfaces and to realize a point-to-point length that matches the one probed in a tactile setup. To that end, we use a collimated incident beam and an imaging system focused on the artifact to record position-resolved images of the reflected intensity. The angle θ is varied by mounting the entire artifact on a rotating platform and recording images of the reflected beam at different rotation angles. This global artifact rotation plays the same role in our interferometer that a shift in the length of the reference arm plays in PSI, allowing independent interferograms to be recorded in parallel at each pixel in the camera image.

To maintain a stable relationship between image and artifact coordinates as the artifact rotates, we use the optical setup of figure 3. A beam splitter mounted on the same rotating platform as the artifact deflects the reflected light toward the camera. The light reaching the camera was reflected an even number of times from co-rotating surfaces, and its direction of travel is thus independent of platform rotation. The rotation of the platform still causes a lateral translation of the outgoing beam, but this can be suppressed at first order by positioning the components such that the offset a between the beam splitter and the rotation axis, measured in the direction of the outgoing beam, matches the distance b between the artifact and the beam splitter. Of course, the condition $a = b$ cannot be satisfied simultaneously at both ends of the etalon since they are at different distances from the beamsplitter. Put another way, the rotation of the artifact leads to a transverse displacement of the wavefront reflected from the back surface relative to the one reflected from the front surface, so the two wavefronts cannot simultaneously have a stable position in the camera image. This leads to a residual relative displacement of the front and back etalon surfaces in the camera image of order θL. As the necessary rotation angles scale as $\theta \sim \sqrt{\lambda/L}$ the residual transverse displacements are of order $\sqrt{\lambda L}$. For our system the residual translation amounts to $\sim$0.1 mm, less than the useful transverse resolution of our images, and is not a problem in practice.

Thus, even as the artifact is rotating relative to the incident beam, the wavefronts which reach the imaging system have a fixed orientation, a nearly fixed transverse position (varying only by $\sim$0.1 mm), and a small and fixed relative angle due only to the imperfect parallelism of the two reflecting surfaces of the etalon. The angular stability and near-parallelism of the interfering wavefronts suppresses parasitic phase shifts due to optical aberrations in the imaging system to a negligible level.

Rather than imaging the reflected beam as described above, one could image the transmitted beam, whose direction is unaffected by the rotation of the artifact. However, the leading-order interference in transmission is between light that went straight through the etalon, without any reflections, and light which was reflected twice, once by each surface. Because the etalon faces are uncoated to avoid undesirable phase shifts, they have a low reflectance ($<4\%$), and the resulting amplitude mismatch between interfering fields leads to very poor contrast. The reflected beam, meanwhile, is dominated by two components of similar amplitude, one reflected from the first surface and one reflected from the second surface, so has nearly full interference contrast. The resulting improvement in signal-to-noise ratio justifies the modest additional complexity of the setup in figure 3.

The rest of the optical setup is standard. Light from a frequency-stabilized HeNe laser at either 543 nm, 612 nm, or 633 nm is delivered to the experiment by single-mode fiber, focused through a 150 µm pinhole, expanded to a beam diameter of 50 mm and collimated by an achromat with a 300 mm focal length before being directed through the beamsplitter to the artifact. The collimation of the beam is checked using a shear plate and its alignment with the artifact is checked by retroflecting light from the artifact through the pinhole. Light deflected by the beamsplitter to the imaging system is collected by another 300 mm-focal-length achromat and then focused by a 50 mm-focal-length plano-convex lens onto a CCD sensor. An iris cuts out stray reflections and background light. Thermistors probe the temperature of the artifact

at three positions on the housing, as well as the air temperature immediately above and behind the artifact. Together with barometer and hygrometer readings taken nearby, this allows a correction for the index of refraction of air using Ciddor's equation [14].

4. Angle-stepping gap interferometry

The interferogram is recorded by rotating the platform through a sequence of angles $\{\theta_k\}$, where $\theta = 0$ corresponds to normal incidence, and recording images at each angle. Neglecting multiple reflections for the moment, the reflected intensity varies as a function of angle as

$$I \propto 1 - \gamma \cos\left(4\pi \frac{L}{\lambda} \cos\theta\right) \tag{2}$$

$$\propto \gamma \cos\left(4\pi \frac{L}{\lambda} + \pi - 8\pi \frac{L}{\lambda} \sin^2\left(\frac{\theta}{2}\right)\right) + 1 \tag{3}$$

where γ is the interference contrast. In the second line the interferogram is recast into the generic form commonly used in PSI: $I = A\cos(\phi_0 + \phi) + B$, with A an interference amplitude, B a background level, ϕ_0 the static phase to be measured and ϕ the adjustable phase introduced by a PSI system [7, 9, 15]. The phase corresponding to the gap length we wish to measure is

$$\phi_0 = 4\pi \frac{L}{\lambda} \tag{4}$$

while the adjustable phase used for the measurement is

$$\phi = \pi - 8\pi \frac{L}{\lambda} \sin^2\left(\frac{\theta}{2}\right) \tag{5}$$

$$\approx \pi - 2\pi \frac{L}{\lambda} \theta^2 \tag{6}$$

with a small-angle approximation in the second line. The leading π term is the phase difference between reflection at glass-to-air and air-to-glass interfaces. It corresponds to the physical fact that the interference must be destructive when $L \to 0$, as there can be no reflection from the gap when the gap vanishes.

Such an interferogram is shown in figure 4. As with Haidinger fringes, the intensity is not a periodic function of angle. The phase depends quadratically on θ and varies more slowly, leading to wider fringes, as the artifact approaches normal incidence ($\theta = 0$). At normal incidence the phase goes through a maximum and the intensity thus goes through a stationary point before reversing the direction of its oscillation. Although the whole interferogram contains information about the length of the artifact, the height of this central extremum is the most obvious qualitative indicator of ϕ_0. If ϕ_0 were an even multiple of π, i.e. if L were a multiple of $\lambda/2$, this central stationary point would be a minimum at the same level as the other minima in the interferogram. If ϕ_0 were an odd multiple of π, it would instead be a maximum at the same level as the other maxima in the interferogram. In this case $\phi_0 \mod 2\pi \approx 0.645\pi$, so the central peak is at around $\frac{1}{2}(1 - \cos 0.645\pi) \approx 72\%$ of the height of the other fringes.

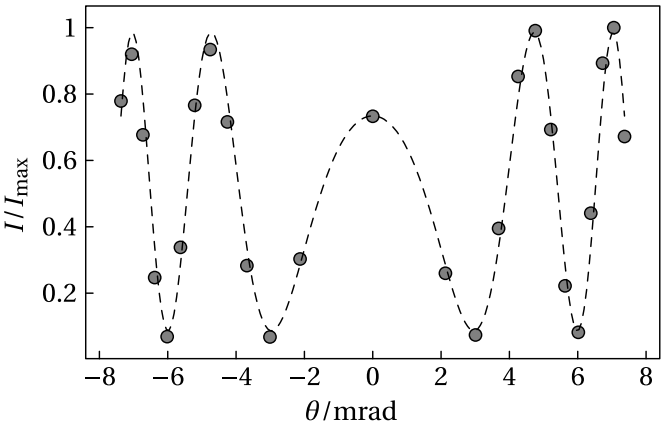

Figure 4. Typical interferogram at a single pixel. Solid dots show reflected intensity recorded by the camera, dashed line shows the ideal interferogram of equation (2). Intensities are expressed relative to the maximum recorded intensity.

Multiple reflections in the etalon produce higher harmonics which distort the interferogram of equation (2), producing an Airy function rather than a simple sinusoid [12, 13]. Thanks to the low reflectance of the uncoated etalon surfaces, however, the amplitude of these harmonics falls off by a factor of ~ 0.04 at each order. The data analysis discussed below takes into account two orders of the distortion, corresponding to light that has made up to two additional round trips in the etalon. The remaining harmonics, with a relative amplitude $<10^{-4}$ compared to the signal, are neglected.

We record camera images at 25 angles distributed over $F = 2$ interference fringes on either side of normal incidence, with $N = 6$ images per fringe. Labeling the images by an integer k we have:

$$\theta_k = \mathrm{sgn}(k) \sqrt{\left|\frac{k}{N}\right| \frac{\lambda}{L}}, \qquad k \in \{-F \cdot N, \ldots, F \cdot N\} \tag{7}$$

$$\phi_k \approx \pi - 2\pi \left|\frac{k}{N}\right|. \tag{8}$$

As in PSI, the recorded intensities are combined using a linear filter to estimate the complex amplitude of the interference signal [7–9]

$$Z = \sum_k w_k I_k. \tag{9}$$

Here the $\{w_k\}$ are the predetermined complex weights of the linear combination and Z is the resulting amplitude estimate. The estimate $\widehat{\phi_0}$ of the phase ϕ_0 is just the argument of this complex amplitude:

$$\widehat{\phi_0} = \arg Z = \arctan\left(\frac{\sum_k \mathrm{Im}(w_k) I_k}{\sum_k \mathrm{Re}(w_k) I_k}\right). \tag{10}$$

The complex weights $\{w_k\}$ are chosen following a procedure similar to that of Hibino [8, 16], by imposing constraints of the form

$$\sum_k w_k \theta_k^p \mathrm{e}^{\mathrm{i}m\phi_k} = 2\delta_{p0}\delta_{m1} \tag{11}$$

where m labels a harmonic of the signal, p labels an order in the Taylor expansion of the corresponding amplitude, and δ_{ij} is the Kronecker delta. The equation with $p=0$ and $m=1$ fixes the filter's sensitivity to an oscillation proportional to $\mathrm{e}^{-\mathrm{i}\phi}$, i.e. the positive-frequency part of the interferogram predicted by equation (2). The other equations with $p=0$ impose that the filter should be insensitive to the background light level ($m=0$), to the counter-rotating term proportional to $\mathrm{e}^{\mathrm{i}\phi}$ ($m=-1$), and to higher harmonics due to multiple reflections in the artifact ($m=\pm2,\pm3$) [7]. Equations with $p=1,2$ impose insensitivity to linear and quadratic drift in the background intensity or in the amplitudes of harmonic components, as well as to small errors in the step size [7, 8, 15, 16]. We solve this linear system of equations numerically to obtain the weights that satisfy all such equations up to $p=2, m=\pm3$, using phase shifts ϕ_k calculated according to equation (5). Representative values of the weights $\{w_k\}$ are given in the appendix.

In principle, one could estimate $\widehat{\phi_0}$ from the height of the central peak relative to the surrounding fringes, without requiring any quantitative knowledge of the angle θ. In practice, the estimator of equation (10) does depend on approximate knowledge of the angles $\{\theta_k\}$, since the weights $\{w_k\}$ implicitly depend on the choice of angles, but the impact of angular errors can be minimized using techniques similar to those used to cope with phase-shift errors in conventional PSI [7, 8, 15, 16]. Choosing weights $\{w_k\}$ that satisfy equation (11) with $p=2$ eliminates the first-order sensitivity to overall scaling errors of the angle. Choosing a set of angles $\{\theta_k\}$ and weights $\{w_k\}$ that are symmetric about $\theta=0$ eliminates the first-order sensitivity to overall angular offset errors, since such constant angular offsets produce odd-symmetric distortions of the interferogram whereas $\widehat{\phi_0}$ depends on the even-symmetric part. Random errors in individual angles θ_k produce phase-dependent errors in $\widehat{\phi_0}$ which we characterize below based on the measurement repeatability with varying ϕ_0. For an artifact with $L=20$ mm, we find that control of the angle θ at the $\sim$1 mrad level, readily achieved using commercially-available rotary tables, suffices for optical length measurements with uncertainties of a few nanometers.

5. Optical measurement results

The measurement procedure is thus to collect camera images for the artifact rotation angles $\{\theta_k\}$ chosen according to equation (7), smooth the images with a 2D Welch filter of 1 mm diameter to suppress diffraction artifacts and camera noise at high spatial frequency, and reconstruct the interference phase at each pixel using the filter of equation (9). The result is a map of variations in the gap between etalon plates as a function of transverse position, as in figure 5. This map shows that the etalon plates are flat and parallel to within

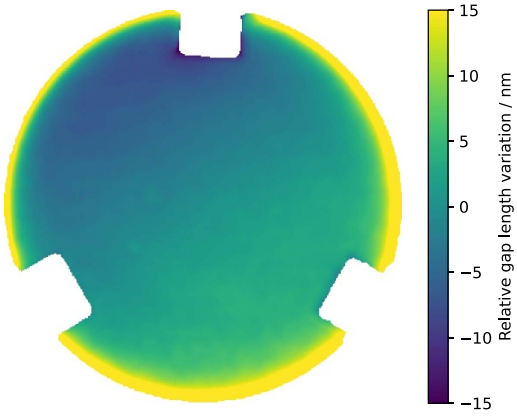

Figure 5. Map of phases estimated from a single angle scan, converted to length variation.

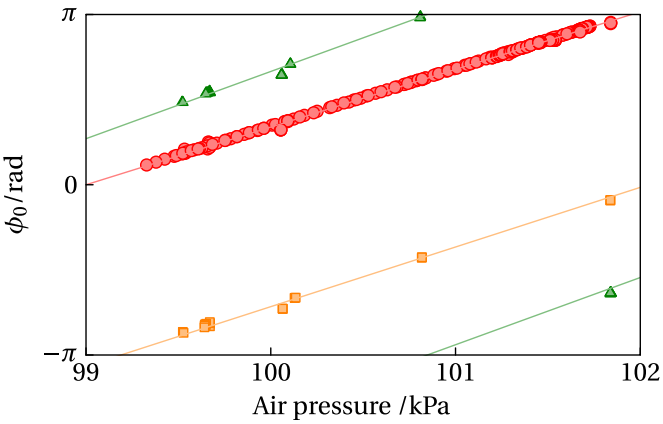

Figure 6. Interference phase at the center of the artifact as a function of ambient atmospheric pressure. Red circles: with a 633 nm HeNe laser. Orange squares: with a 612 nm HeNe laser. Green triangles: with a 543 nm HeNe laser.

10 nm over most of their area, with some rolloff at the edges, three gaps in the data corresponding to the three pillars, and a few ring-shaped diffraction patterns due to dust particles in the imaging optics.

Figure 6 shows the phase of the central pixel for each of an ensemble of 285 maps collected over a period of 42 months. Plotted as a function of atmospheric pressure, the phases fall on three lines, one for each wavelength used, showing that the dominant influence on the recorded phase is the changing atmospheric index of refraction. Non-linear errors in phase determination would distort these lines, and the absence of such distortions indicates that the chosen weights $\{w_k\}$ adequately suppress all relevant harmonics in the interferogram.

Taking the phase readings of figure 6, correcting the calibrated laser vacuum wavelengths using the empirical formulae of Ciddor for the refractive index of air [14], and reconstructing the integer part of the fringe order by the method of excess fractions using the three laser wavelengths [13, 17], we obtain 285 estimates of the central length L, which are plotted in figure 7 as deviations from the nominal artifact length of 20 mm. The method of excess fractions requires some prior

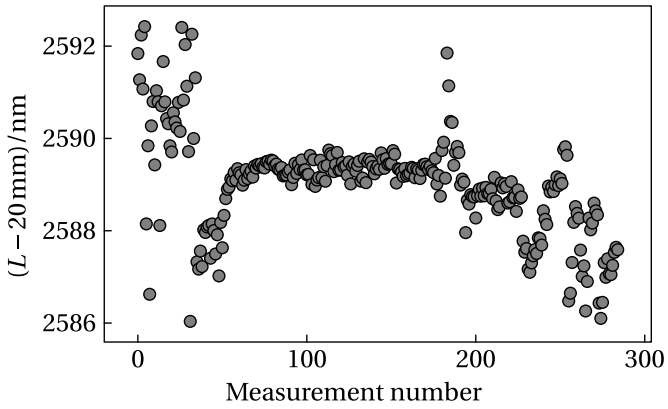

Figure 7. Central length deviations from the 20 mm nominal artifact size, calculated for each of 285 phase maps.

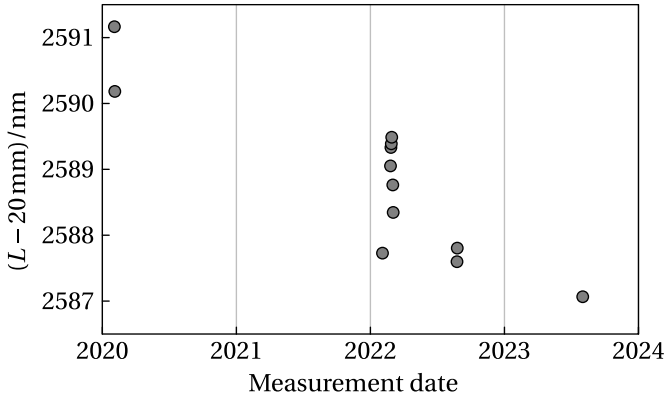

Figure 8. Average central length deviation from 20 mm calculated for each measurement day in a period of 42 months.

knowledge of L, but given our phase measurement uncertainty and choice of lasers a prior estimate with a standard uncertainty $u \approx 10$ µm suffices [18]. A preliminary measurement made with a CMM easily meets this requirement.

The first 30 measurements are especially noisy due to a misaligned optical fiber that produced excess intensity fluctuations. Even including this data, the entire history, which covers multiple reassemblies and realignments of the optical setup, the use of two different rotary tables, and measurements by multiple operators, fits in a 7 nm-wide band.

The laboratory's climate-control system is shut down for maintenance every six months, leading to week-long temperature excursions of ca. 6 °C. The 42 month measurement history summarized in figure 7 thus includes any effects of hysteresis in the artifact due to temperature cycling on this scale.

Plotting the average of all measurements conducted on a given day as a function of date makes it easier to see long-term trends (figure 8). This suggests that the artifact may be contracting by around ≈ 1 nm yr^{-1}. We cannot confidently distinguish such a drift rate from zero given our current uncertainties, so we provisionally treat the artifact length as constant and include putative drift in our uncertainty estimates.

6. Tactile measurement

To test its suitability for tactile measurement, the etalon was measured using a Mitutoyo Legex 707 CMM equipped with an MPP310 tactile probe. The measurement was a direct comparison to an internal-length artifact consisting of two end-caps wrung to a calibrated 20 mm gauge block. The two artifacts were mounted side by side with their measurement axes parallel to each other and aligned with the machine X axis (bridge traversal). The artifacts were aligned so that their gauging faces were at the same position along the X scale to minimize the impact of scale non-linearities. Due to the flexible mounting of the etalon in its housing, the default 80 mN contact force of the tactile probe displaced the etalon assembly by several hundred nanometres. Measurements were therefore made at several different contact force settings, from 30 mN to 160 mN, to allow an extrapolation to the undeflected length that would be measured at zero applied force. The gauging faces of the two cap blocks in the gauge-block artifact, meanwhile, were out of parallel by ≈5 µrad, introducing an Abbe error as in figure 1(c). Measurements were thus taken at multiple Abbe offsets from 20 mm to 30 mm to allow an extrapolation back to the calibrated central length of the gauge block.

Treating the CMM measurement as an independent determination of the length of the etalon, with traceability through the calibrated gauge block, yields a result $L - 20\,\mathrm{mm} = 2.49\,\mu\mathrm{m} \pm 0.13\,\mu\mathrm{m}$, where the uncertainty is quoted at coverage factor $k = 2.03$ corresponding to 95% confidence. The difference between this tactile result and the interferometric results plotted in figure 8 is −100 nm ± 130 nm, consistent with zero given the tactile measurement uncertainties.

7. Uncertainty budgets

Tables 1–3 present the major contributors to the uncertainty budget, and the associated effective degrees of freedom, for three different measurement scenarios. Table 1 considers only the angle-stepping measurement, with a measurand defined as the separation of the *optical* surfaces of the etalon. This gives the uncertainty relevant for comparisons between angle-stepping measurements at different times, e.g. to assess secular drift in figure 8. In table 2 we consider the use of the etalon as a transfer standard in our CMM, where the uncertainties of the tactile probing system and the differences between optical and mechanical surfaces become important. Finally table 3 considers the uncertainty of the comparison conducted in section 6, which involved a gauge block with wrung endcaps as in figure 1(c).

The repeatability of the purely optical measurement was estimated from the standard deviation of all 285 length measurements in the dataset. This is a conservative estimate since it includes excess noise due to optical fiber misalignment in the first 30 measurements as well as possible contributions from secular change in the artifact. The raw phase measured by the interferometer varied due to air pressure fluctuations as well as the use of multiple laser wavelengths, so this repeatability is assumed to cover phase-dependent non-linear errors in the

Table 1. Optical measurement uncertainty budget.

Contributor	u	ν_{eff}
Repeatability	1.1 nm	284
Face parallelism	0.7 nm	94
Thermal distortion	0.6 nm	50
Refractive index	$L \times 71\,\text{nm}\,\text{m}^{-1}$	58
Source size	$L \times 16\,\text{nm}\,\text{m}^{-1}$	50
Vacuum wavelength	$L \times 9\,\text{nm}\,\text{m}^{-1}$	5
Artifact alignment	$L \times 6\,\text{nm}\,\text{m}^{-1}$	50
Total: $\sqrt{(1.4\,\text{nm})^2 + (L \times 73\,\text{nm/m})^2} = 2.0\,\text{nm}$		217

interferometer, including those due to fourth-harmonic distortion and to errors in the rotation angles $\{\theta_k\}$.

To check more specifically for wavelength-dependent effects, we have computed the average result separately for each wavelength on each measurement day. The standard deviation over wavelengths, pooled across the six days when all three wavelengths were used, is 0.6 nm. This pooled standard deviation is about what we would expect based on the estimated single-measurement repeatability of 1.1 nm and the fact that there were typically three readings contributing to each single-wavelength single-day average. Thus, we see no evidence for specifically wavelength-dependent bias at the $\sim$ 1nm level.

The uncertainty due to face parallelism is based on the standard deviation of the lengths measured at all pixels within 2mm of the designated gauging point. A similar result can be obtained by fitting planes to the phase maps to estimate the parallelism of the etalon faces ($\approx$0.7 µrad) and computing the resulting length distribution for positions uniformly distributed in a disk with a 2 mm radius around the gauging point.

Although the thermal expansion of the ULE spacers is negligible in such a short artifact, the mismatch in thermal-expansion coefficients at the contact patch between the fused-silica etalon end plates and the ULE spacers might lead to temperature-dependent deformations of the artifact. There might also be distortions due to forces exerted by the expanding aluminium housing through the elastic mounting to the etalon. Based on the correlation of temperature with measured length in a sample of 219 measurements taken over the temperature range from 19.92 °C to 20.18 °C in the winter of 2022, we estimate that any such distortions must have an effect on the central length $<7\,\text{nm}\,\text{K}^{-1}$, corresponding to a length uncertainty $u = 0.6$ nm given the typical temperature fluctuations in our setup.

The other significant contribution to the optical measurement uncertainty is due to the impact of temperature gradients around the artifact on the index-of-refraction correction. We estimate the scale of these gradients from the total spread of readings from the 5 thermistors, which is below 250 mK for all measurements. Other length-dependent contributions have only a minor effect for our 20 mm artifact, and the resulting combined standard uncertainty is 2.0 nm for the purely optical measurement.

Table 2. Uncertainty budget for the use of the etalon as a transfer standard in our CMM.

Contributor	u	ν_{eff}
Extrapolation to zero force	37 nm	11
CMM scale resolution	2.9 nm	1000
Phase correction	2.8 nm	12
Optical measurement	2.0 nm	217
Thermal expansion	1.4 nm	25
Total	37 nm	11

Table 3. Uncertainty budget for the comparison of the etalon to a calibrated gauge block.

Contributor	u	ν_{eff}
Extrapolation to gauge centreline	42 nm	11
Etalon as tactile transfer standard	37 nm	11
CMM error map variation	23 nm	20
Calibration of gauge block	15 nm	50
Thermal expansion of gauge block	6 nm	13
Total	63 nm	33

The intended use of the etalon is as a transfer standard for tactile measurement systems, and in that context the tactile system's ability to realize the same measurand as the angle-stepping measurement becomes important. Table 2 summarizes the relevant uncertainty contributions for the use of the etalon as a transfer standard in our CMM. The largest of these is simply the repeatability of the CMM system, including the repeatability of the probing force, which has a large effect in this case due to the flexible mounting of the etalon in its housing. Based on fit residuals, the combined effect of position and force repeatability on the extrapolated length at zero contact force is estimated to be $u = 37$ nm for our probing system. The remaining contributions would become significant only if this repeatability were substantially improved, e.g. with better fixturing to lower the sensitivity of the measured length to probing forces. Besides the optical measurement uncertainties discussed above, these other contributions include the resolution of the scales in the CMM, the phase correction relating the plane of optical reflection to the plane of mechanical contact, and thermal distortions. The phase correction in particular is a crude estimate, based on literature values for the thicknesses of adsorbed films [19, 20] and for the impact of surface roughness [21, 22]. If the etalon were to be used in a tactile system capable of sub-10 nm resolution, then a more detailed study of the probing system's interaction with the etalon surface would be called for [23].

Finally, the comparison of the etalon length to a calibrated gauge block described in section 6 involves all the usual uncertainties of comparison measurements using gauge-block stacks as a reference, the most important of which are listed in table 3. Since we are comparing internal lengths, there

is a significant contribution due to the extrapolation from a measurement line outside the reference gauge block (see figure 1(c)) to a calibrated central length running through the gauge block. This uncertainty was estimated from fit residuals to an ensemble of measurements conducted at different Abbe offsets and probing forces. The uncertainty of the measurement on the etalon measurement is taken from table 2. Another significant contribution comes from imperfections in the CMM controller's error map: the length of an artifact, measured along the machine X axis, depends on corrections applied by the controller error map which in turn depend on the position in the Y and Z axes. Since the two artifacts being compared do not physically occupy the same position, the result is an uncertainty on the length comparison even when their faces are carefully aligned to the same X-axis position, which we estimate based on studies of comparisons between matched gauge-block pairs. Calibration and thermal expansion uncertainties of the gauge block play comparatively minor roles, though both are substantially larger than the corresponding uncertainties for the etalon.

8. Outlook

We have presented an end standard and a simple interferometric measurement technique designed to minimize the mismatch between interferometric and tactile two-point length measurements, and thus to reduce the uncertainty of bidirectional corrections. The observed reproducibility of the interferometric measurements over a 42-month period of ongoing development is well within the estimated optical measurement uncertainty of $U = 4$ nm.

Compared to a measurement based on a white-light interferometer, this setup avoids the need for a translation stage, whose straightness errors would masquerade as spurious nonparallelism of the etalon faces. Further, because the interference is formed between the etalon faces, we avoid wavefront errors due to imperfections in the beam-splitter or reference reflector of an external interferometer. The price paid for this simplicity is the need for additional stabilized laser wavelengths to implement the method of excess fractions.

The uncertainty of the optical measurement is substantially better than the repeatability of the probing system on our CMM, so the most important improvements are those that would reduce the uncertainty in the mechanical measurement. In particular, a more rigid mounting of the artifact in its housing would reduce the sensitivity to probing forces and allow a more accurate extrapolation to zero force.

We thank S.L.S. Optics for manufacturing the custom etalon used in this work.

Appendix. Coefficients

The linear filter weights $\{w_k\}$ used to reconstruct the interference amplitude Z according to equation (9) are calculated numerically for each measurement. This allows us to correct for known deviations from the ideal frame angles, whether due to positioning errors in the rotary table, the approximations of equations (6) and (8), or the use of approximate wavelengths to calculate frame angles at data-taking time. In practice, however, these corrections are small and uniform, and the fixed set of coefficients given in table 4 could have been used for all the measurements with a negligible impact on the results.

Table 4. Typical filter coefficients $\{w_k\}$. For each frame index, the table lists the intended phase shift in fringes and the real and imaginary parts of the associated filter weight. $k = 0$ when the etalon faces are normal to the light beam. Weights for negative k are given by the symmetry $w_{-k} = w_k$.

k	$\phi_k/2\pi$	$\mathrm{Re}(w_k)$	$\mathrm{Im}(w_k)$
0	3/6	−0.184	−0.096
1	2/6	−0.097	−0.169
2	1/6	0.111	−0.192
3	0/6	0.250	0.000
4	−1/6	0.139	0.241
5	−2/6	−0.153	0.265
6	−3/6	−0.149	0.096
7	−4/6	0.014	0.024
8	−5/6	−0.028	0.048
9	−6/6	−0.083	−0.000
10	−7/6	−0.055	−0.096
11	−8/6	0.070	−0.120
12	−9/6	0.074	−0.048

ORCID iD

Brian J Eves https://orcid.org/0000-0003-2481-0334

References

[1] Konda Y, Hirai A and Youichi B 2022 Two-point diameter calibration of a sphere using a micro-coordinate measuring machine at NMIJ *Metrologia* **59** 024005
[2] International Standard 3650:1998 1998 *Geometrical Product Specifications — Length Standards — Gauge Blocks* International Organization for Standardization
[3] Doiron T, Everett D, Faust B, Stanfield E and Stoup J 1998 The case against optical gage block metrology *Proc. SPIE* **3477** 188–98
[4] Doiron T 2008 Gauge blocks — a zombie technology *J. Res. NIST* **113** 175–84
[5] Stanfield E, Stoup J, Braine M and Doiron T 2020 Sphere diameter interferometry with nanometer uncertainty *Metrologia* **57** 025003
[6] Terrien J 1959 Perfectionnements à l'emploi d'un ensemble photomultiplicateur-interféromètre de Michelson pour les mesures de longueur d'onde et de profil spectral des radiations optiques de grande finesse *Opt. Acta* **6** 301–7
[7] Surrel Y 1996 Design of algorithms for phase measurements by the use of phase stepping *Appl. Opt.* **35** 51–60
[8] Hibino K, Oreb B F, Farrant D I and Larkin K G 1995 Phase shifting for nonsinusoidal waveforms with phase-shift errors *J. Opt. Soc. Am.* A **12** 761–8
[9] Servin M, Estrada J C and Quiroga J A 2009 The general theory of phase shifting algorithms *Opt. Express* **17** 21867–81
[10] Thalmann R 2000 EUROMET key comparison: cylindrical diameter standards *Metrologia* **37** 253–60

[11] Bánréti E 2010 Final report on EUROMET key comparison EUROMET.L-K4: calibration of diameter standards, group 2 *Metrologia* **47** 04001
[12] Benoît J-R, Fabry C and Pérot A 1913 Nouvelle détermination du rapport des longueurs d'onde fondamentales avec l'unité métrique *Travaux et mémoires du B.I.P.M.* **XV** 1–134
[13] Born M and Wolf E 1980 *Principles of Optics* 6th edn (Pergamon)
[14] Ciddor P E 1996 Refractive index of air: new equations for the visible and near infrared *Appl. Opt.* **35** 1566–73
[15] Surrel Y 1997 Design of phase-detection algorithms insensitive to bias modulation *Appl. Opt.* **36** 805–7
[16] Hibino K, Oreb B F, Farrant D I and Larkin K G 1997 Phase-shifting algorithms for nonlinear and spatially nonuniform phase shifts *J. Opt. Soc. Am.* A **14** 918–30
[17] Benoît R 1898 Application des phénomènes d'interférence à des déterminations métrologiques *J. Phys. Theor. Appl.* **7** 57–68
[18] Leroux I D 2021 Choosing wavelengths and assessing blunder risk for the method of exact fractions *Metrologia* **58** 014004
[19] Busch I *et al* 2011 Surface layer determination for the Si spheres of the Avogadro project *Metrologia* **48** S62–S82
[20] Asay D B and Kim S H 2005 Evolution of the adsorbed water layer structure on silicon oxide at room temperature *J. Phys. Chem.* B **109** 16760–3
[21] Thwaite E G 1978 Phase correction in the interferometric measurement of end standards *Metrologia* **14** 53–62
[22] Shutoh S, Moriyama H and Sawabe M 1998 Phase shift on ceramic gauge blocks *Proc. SPIE* **3477** 181–6
[23] Balling P, Ramotowski Z, Szumski R, Lassila A, Křen P and Mašika P 2019 Linking the optical and the mechanical measurements of dimension by a Newton's rings method *Metrologia* **56** 025008